



Statistical analysis of measured and computed thickness and interfacial temperature of free-falling turbulent liquid films



Nikhin Mascarenhas, Issam Mudawar*

Purdue University Boiling and Two-Phase Flow Laboratory (PU-BTPFL), School of Mechanical Engineering, 585 Purdue Mall, West Lafayette, IN 47907, USA

ARTICLE INFO

Article history:

Received 10 October 2013

Received in revised form 18 February 2014

Accepted 19 February 2014

Available online 19 March 2014

Keywords:

Falling films

Waviness

Turbulence

Probability density

Covariance

Spectral analysis

ABSTRACT

This study examines the evolution of film thickness and interfacial temperature in turbulent, free-falling water films that are subjected to sensible heating. Measured temporal records of film thickness and interfacial temperature are subjected to thorough statistical analysis to understand the influence of interfacial waves on the distribution, periodicity and interdependence of these two parameters. A computational model of the film is constructed and its predictions subjected to similar statistical analysis. The statistical tools employed in this study include probability density, auto-covariance, cross-covariance, auto-spectrum and cross-spectrum. Probability density of film thickness shows an increase in substrate thickness and amplitude with increasing Reynolds number, while auto-covariance of thickness captures dominant frequencies corresponding to the large waves. Cross-covariance of film thickness and interfacial temperature difference captures a clear phase shift between the two parameters, with the temperature reaching a maximum in the relatively thin film region between the substrate and wave peak. Statistical results for both parameters exhibit clear dependence on axial location in the thermal entrance region, and point to fully developed wave structure downstream. The statistical results based on computed film thickness and interfacial temperature difference agree well with the results based on the measured, which demonstrates the effectiveness of the adopted computational tools at predicting the complex transport phenomena associated with wavy liquid–vapor interfaces.

© 2014 Elsevier Ltd. All rights reserved.

1. Introduction

Gravity-driven two-phase systems are very popular in many industries because of their ability to achieve very high heat transfer coefficients while avoiding the penalty of high pressure drop. These systems include pool boiling thermosyphons [1,2] and pumpless gravity driven loops [3,4].

Free-falling liquid films are found in another type of gravity-driven systems that feature high heat transfer coefficients, which include condensers, evaporators, spray-type refrigerators, distillation columns, chemical reactors, and nuclear reactors. The attractive thermal attributes of free-falling liquid films are realized by minimizing conduction resistance for thin laminar films and capitalizing upon both turbulent fluctuations (for high film flow rates) and added mixing provided by interfacial waves. But despite many decades of efforts to model the transport characteristics of free-falling films, uncertainty remains concerning the dampening of turbulent eddies at the film interface due to surface tension, tran-

sition from laminar to turbulent flow, and, most importantly, the influence of interfacial waves.

1.1. Interfacial characteristics of falling films

Liquid films found in thermal devices are typically thin, exhibit turbulent flow and rely on gravity to achieve fluid motion. The afore-mentioned attributes of films are highly complicated by the prevalence of interfacial waves spanning a broad range of speeds and length scales. At a first glance, time records appear to show large waves that have a profound influence on temperature distribution across the film as shown in Fig. 1(a) and (b). However, there are appreciable variations in shape, speed and frequency of occurrence of these large waves, in addition to seemingly highly stochastic smaller waves, some of which are superimposed on the large waves.

In a recent study by the authors of the present study [7], time records of film thickness were inspected and repeatable wave patterns identified for different film Reynolds numbers in pursuit of time-averaged values for film thickness, heat transfer coefficient, and both temperature and eddy diffusivity profiles across the film.

* Corresponding author. Tel.: +1 765 494 5705; fax: +1 765 494 0539.

E-mail address: mudawar@ecn.purdue.edu (I. Mudawar).

URL: <https://engineering.purdue.edu/BTPFL> (I. Mudawar).

Nomenclature

C	cross-covariance	x	axial coordinate
C_{μ}	turbulence model constant	y	coordinate perpendicular to the wall
D_H	hydraulic diameter		
f	frequency	<i>Greek Symbols</i>	
g	gravitational acceleration	α	thermal diffusivity
k	thermal conductivity; turbulent kinetic energy	Γ	mass flow rate per unit film width
L	total number of lags in auto-spectra and cross-spectra	δ	film thickness
N	number of discrete data points	Δ	difference between adjacent covariance values
n	number of samples in subset of data record	ε	dissipation rate of turbulent kinetic energy
P	pressure; probability	μ	dynamic viscosity
p	probability density	ν	kinematic viscosity
Pr	Prandtl number	ρ	density
Pr_t	turbulent Prandtl number	σ^2	variance
q_w''	wall heat flux	τ	time lag
r	radial coordinate		
R	auto-covariance	<i>Subscripts</i>	
Re	Reynolds number, $Re = 4\Gamma/\mu$	i	film interface
S	auto-spectrum	in	inlet
s_{ij}	fluctuating component of strain rate tensor	min	minimum
T	temperature	s	solid
t	time	t	turbulent
u	velocity	w	wall
U	inlet streamwise velocity		
u_r	r -direction velocity component	<i>Superscripts</i>	
u_x	x -direction velocity component	—	average
V	inlet normal velocity	+	non-dimensionalized
W	cross-spectrum	'	fluctuating component
w	window function in auto-spectra and cross-spectra		

A closer examination of the time records for large waves in a subsequent study [5] revealed (i) both periodic and non-periodic interfacial features, and (ii) a strong correlation between film thickness and liquid temperature with an identifiable phase shift as shown in Fig. 1(a). These findings clearly point to the need to further explore the interfacial behavior of films using statistical tools. Such tools can be quite effective at identifying any salient and/or repeatable aspects of interfacial behavior.

1.2. Statistical description of interfacial behavior

Phillips [8] studied the structure of waves generated by wind blowing over a large area of the ocean for a long duration and determined statistics for small-scale components of the wave. A statistical equilibrium range in the wave height spectrum was identified and subjected to dimensional analysis to assess the influence of gravity and wavelength of small waves on the magnitude of the spectrum. Telles and Dukler [9] inspected the interfacial structure of a liquid film that is shear-driven by a gas flow by tracking film thickness fluctuations using electrical conductivity methods. A significant portion of the film was comprised of large stable liquid humps – large waves – marred by smaller waves that lost their identity over small distances. Statistical methods were implemented to calculate wave speed, separation distance between humps, amplitude, frequency, and wave shape, for Reynolds numbers as high as $Re = 60,000$. Chu and Dukler [10] further refined these methods and compared them to predictions of a theory they developed for mean substrate thickness and substrate flow rate. This enabled them to demonstrate the importance of the substrate in controlling the film's transport processes. Using probability density distribution of film thickness for high Re , Chu and Dukler [11] showed that the film possessed bimodal characteristics

consisting of large and small waves. They also concluded that large waves dominate transport characteristics in the film, while small waves control transport characteristics in the gas.

Use of statistical methods to decipher salient flow characteristics is well recognized in two-phase research. Aside from temporal fluctuations in key flow parameters, two-phase flow measurements are complicated by intermittence between the two phases. Jones and Delhaye [12] reviewed the experimental techniques used to measure two-phase flow parameters, and emphasized the importance of employing statistical tools to tackle the complex temporal characteristics of the measured parameters. Takahama and Kato [13] used needle contact and electrical capacitance probes to measure the thickness of falling films, and showed that interfacial waves can be effectively characterized over broad flow rate ranges using normal, logarithmic normal and gamma probability distributions of film thickness. Nencini and Andreussi [14] employed statistical methods to analyze experimental data for annular two-phase downflow. Statistical analysis of the large waves and substrate yielded flow rates that agreed well with the actual flow rates. Karapantsios et al. [15] performed a comprehensive experimental and statistical study of falling films. Film thickness data measured for $Re = 509–13,090$ with a wire conductance technique were subjected to statistical analysis using probability density, spectral density, skewness and kurtosis. Lyu and Mudawar [6] performed experiments to investigate the relationship between film thickness and water film temperature for various film Reynolds numbers. Using statistical tools, the relationship between the two variables was shown to be stronger at high compared to low heat fluxes. A cross-spectrum analysis showed a distinct band of dominant frequencies in the relationship between the two variables. Ambrosini et al. [16] used capacitance probes to measure the thickness of water films falling freely down vertical and inclined

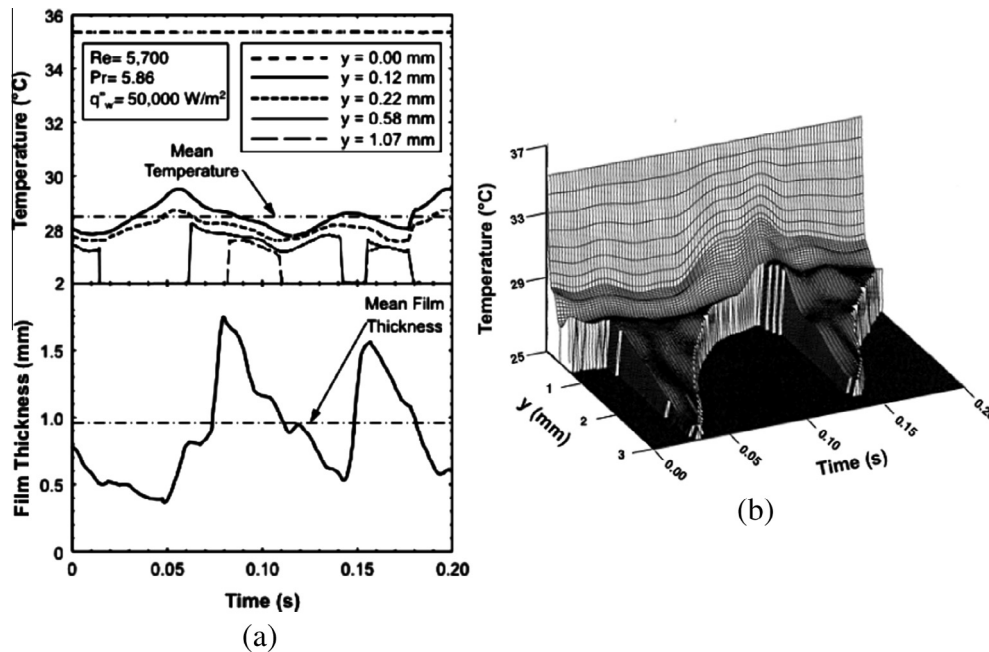


Fig. 1. Measurements at $x = 278$ mm for free-falling water film subjected to sensible heating with $Re = 5700$, $Pr = 5.86$ and $q''_w = 50,000$ W/m²: (a) temporal records of liquid temperature and film thickness (adapted from [5]), and (b) three-dimensional plot of liquid temperature variations with distance from the wall and time (adapted from [6]).

surfaces for a range of Reynolds numbers encompassing both transition and turbulent flows. They collected film thickness time series and used statistical tools to determine mean, minimum and maximum film thickness and wave velocity, and presented power spectra as functions of film flow rate, plate inclination and film temperature.

The present study employs statistical tools to explore the transport behavior of turbulent free-falling liquid films that are subjected to sensible heating. Given the aforementioned importance of interfacial waves on the film's mass, momentum and heat transfer characteristics, these statistical tools are used to investigate temporal records of both film thickness and interfacial temperature, as well as the relationship between the interfacial wave characteristics and those of liquid temperature. The same statistical tools are also applied to temporal records of the film computed using FLUENT. The statistical results based on the measured and computed records are used to validate the effectiveness of computational methods at capturing the correct interfacial profile and influence of waves on the film's transport characteristics. A variety of statistical tools are employed for this purpose. Probability density is used to capture dominant ranges of film thickness and liquid temperature. Auto-covariance and cross-covariance are employed to describe the interdependence between waves and liquid temperature, and auto-spectra and cross-spectra to segregate wave frequencies in pursuit of identifying large and small waves.

2. Experimental methods

The data utilized in this study were obtained from measurements made using the Purdue University Boiling and Two-Phase Flow Laboratory (PU-BTPFL) falling film facility. This facility has yielded data for liquid films subjected to sensible heating [5–7,17–19], evaporation [20] and boiling [21]. Two distinct sets of film thickness instrumentation tools are used in this facility. The first, which is described in [7], provide time-averaged measurements of wall and mean film temperatures. The second, which are used to measure simultaneous instantaneous film thickness and temperature profile, are detailed in [5] and described briefly

below, are employed in measuring the data discussed in the present study. The data for turbulent free-falling water films subjected to sensible heating are examined with the aid of several statistical tools and compared to computational predictions.

Fig. 2(a) shows the central component of the falling film facility, a test chamber where the falling film is generated on the outside wall of a vertical 25.4-mm diameter test section. The test section is comprised of three portions. The film is formed by passing water through the porous wall of a 300-mm long polyethylene tube. The film is formed gradually on the outside wall of the porous tube, which is followed by a 757-mm long adiabatic G-10 plastic tube, over which the film is allowed to develop hydrodynamically. The film is heated along the lower 781-mm long stainless steel tube, which is electrically heated by a d.c. power source to supply a uniform wall heat flux to the film.

As shown in Fig. 2(a), 17 pairs of type-T thermocouples are inserted along the length of the stainless steel tube to measure the inside wall temperature. Axial distance between thermocouples is smaller near the top of the stainless steel tube compared to downstream in order to capture thermal entrance effects. At each axial location, the thermocouples pairs at each axial location are placed diametrically opposite to one another to capture and correct any asymmetry resulting from vertical misalignment. Fig. 2(b) details the construction of the wall thermocouples. Each thermocouple bead is embedded in a small mass of thermally conducting boron nitride epoxy that is deposited into the head of a 6–32 nylon socket head cap screw. The outer surface of the boron nitride is carefully machined to match the curvature of the inner wall of the stainless steel tube. The screw is inserted radially into an inner thermally insulating tube made from Delrin plastic. A small spring maintains positive pressure between the boron nitride epoxy and stainless steel tube.

Fig. 2(c) shows the flow loop that supplies deionized water to the test chamber at carefully regulated flow rate, temperature and pressure. The water is deaerated in a stainless steel reservoir fitted with immersion heaters and a reflux condenser before being charging into the flow loop.

Instantaneous film thickness, film temperature profile and wave velocity measurements are made with the aid of several delicate

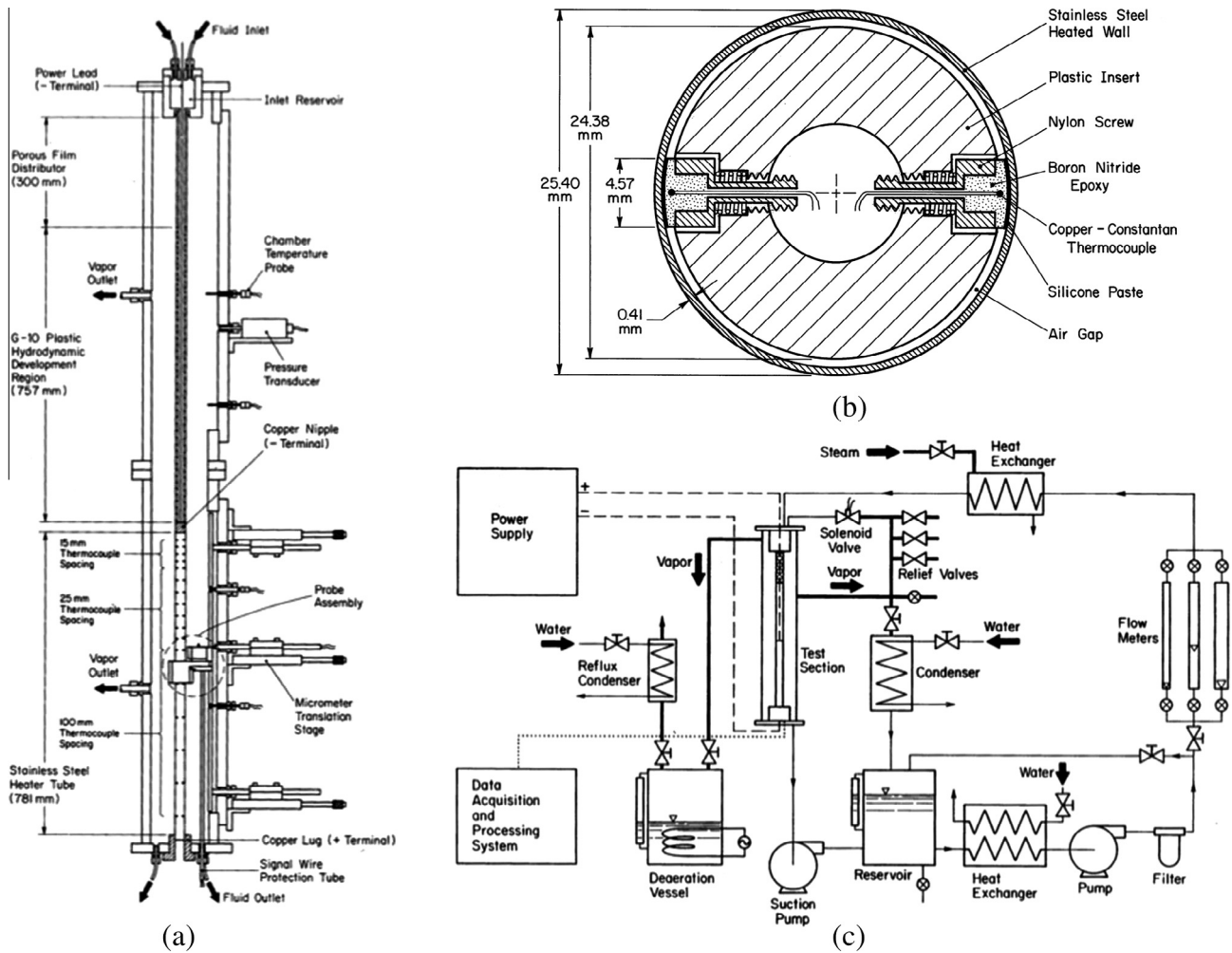


Fig. 2. (a) Cut-away view of test chamber. (b) Cross-sectional view of inner thermocouples. (c) Schematic diagram of flow loop.

probes that are mounted on an assembly block as shown in Fig. 3(a). The block itself is centered around the stainless steel tube by means of six alignment screws that are situated downstream of the probes to preclude any influence to the film measurements. Axial movement of the block is aided by a vertical guide rail, which is connected to two external micrometer translation stages that control the assembly block's horizontal position. The probes consist of a thermocouple array, thickness probe and a thickness calibration probe, all mounted in the same horizontal plane. A second thickness probe used for wave velocity measurements is situated 29.7 mm downstream with a 41° azimuthal offset to avoid the influence of wakes created by the upstream probes.

The thermocouple array is further detailed in Fig. 3(b), which shows twelve type-E 0.0762-mm diameter thermocouple beads made from 0.0508 mm wire that are distributed over a 5-mm span from the heated wall, supported on a G-10 fiberglass plastic knife-edge. Thermocouple locations are denser near the stainless steel wall to capture the near-wall thermal boundary layer. A protrusion on the downstream edge of the plastic knife-edge plate prevents the instrumented portion from making direct contact with the wall. The maximum standard deviation of temperature fluctuation for each thermocouple is 0.17 °C, which is dictated by the high speed data acquisition system. The thermocouples are calibrated in a constant temperature bath at several temperatures. This is achieved by filling the lower portion of the test chamber with water with the probe assembly block completely submerged. Electrical current is then supplied across the stainless steel tube to the

same heat flux levels applied during the subsequent falling film experiments to calibrate the thermocouples for offset resulting from the d.c. current. The calibration procedure is repeated several times after using each batch of deionized water in the falling film configuration to maintain thermocouple offset below 0.2 °C.

The primary thickness probe used for instantaneous film thickness measurement is based on the principle of hot-wire anemometry. Shown in Fig. 3(c), this probe is made from 0.0254-mm diameter platinum-10% rhodium wire that is extended across the liquid-vapor interface. A constant d.c. current is supplied through the wire, and film thickness inferred from variations in the probe's voltage drop. This technique takes into account the large ratio of heat transfer coefficient along the portion of probe wire submerged in liquid compared to that in vapor, as well as the relationship between electrical resistance and temperature. Once calibrated, passage of a constant current through the probe wire yields a voltage drop that is a function of the length of wire submerged in liquid alone.

Extensive calibration is required to ensure accurate film thickness measurement. This includes first submerging the probe vertically downward in a small test cell containing a stagnant layer of water to generate the linear dependence of voltage drop on water layer thickness. This is followed by in situ calibration that is performed prior to each test at heating conditions identical to those of the test itself using the calibration probe shown in Fig. 3(c). The measurement resolution and response time of the thickness probe are 0.05 mm and 0.14 ms, respectively [19].

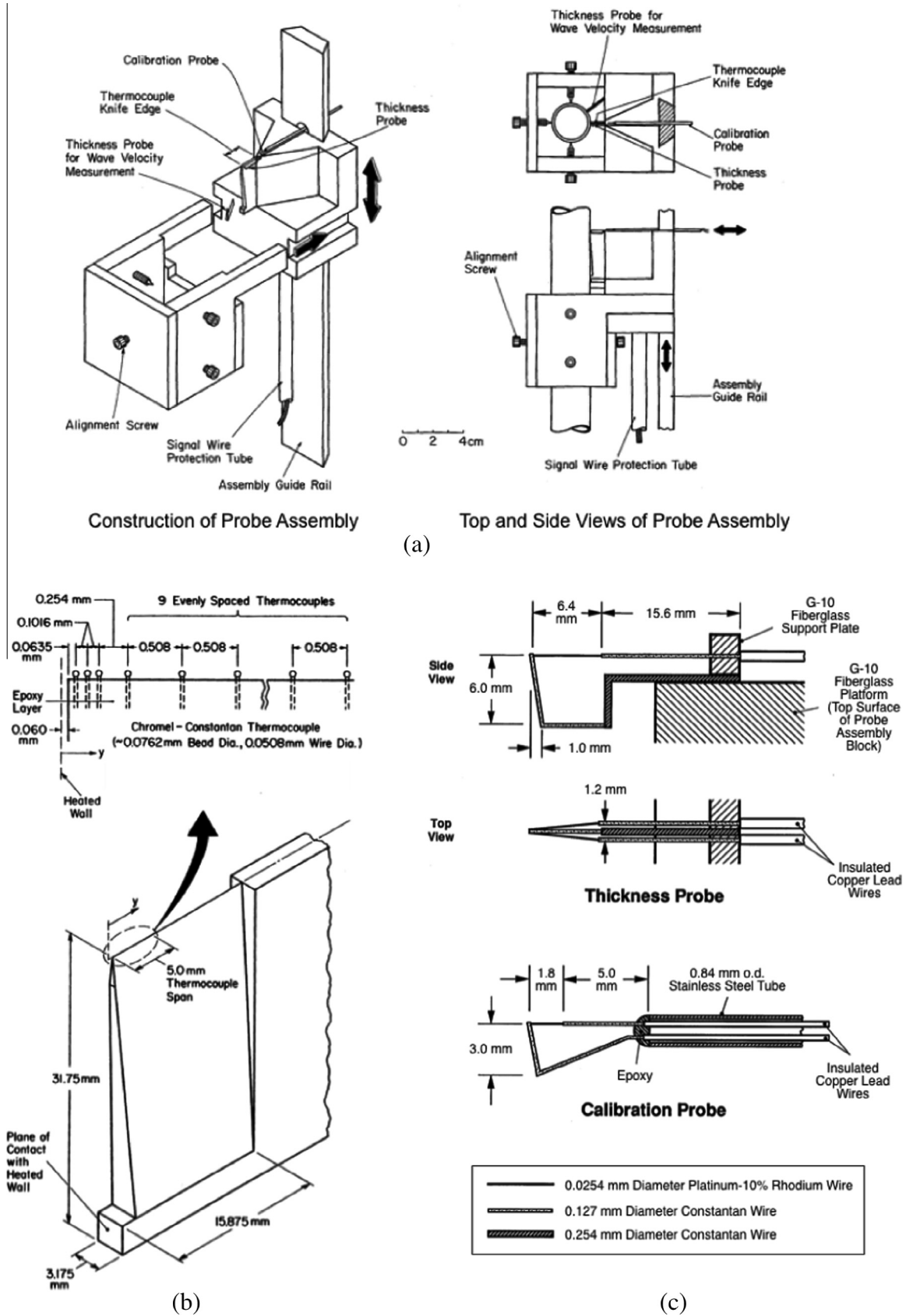


Fig. 3. Construction of (a) probe assembly, (b) thermocouple knife-edge, and (c) thickness probe and thickness calibration probe.

Instantaneous temperature measurements across the film are made simultaneously with the film thickness measurements over a sampling period of 1 s at a frequency of 500 Hz. The temperature data are low-pass filtered using a fourth order 0.1 dB Chebyshev digital filter code written by Walraven [22].

3. Numerical methods

Falling film tests performed using the experimental methods described in the previous section are simulated using the FLUENT Analysis System in the Toolbox of ANSYS Workbench 14.0.0 [23]. In recent years, the flow modeling capability of FLUENT has been expanded by researchers to enhance turbulence prediction and include two-phase flows and phase change [24–30]. In the present study, the Project Schematic of Workbench in ANSYS FLUENT 14.5 is utilized to construct and mesh the thermally active flow domain, as well as to generate and extract instantaneous data that can be compared to the measurements.

Fig. 4 shows the computational domain, a 2-dimensional axisymmetric system, which is justified by the small film thickness. The key components of the domain are the inlet reservoir, porous film distributor, and 1835-mm long annulus formed between the outer wall of the 25.4-mm test section and inner walls of the test chamber. An annulus thickness is assigned to yield a flow area equal to the actual flow area between the test section and test chamber walls.

The computation utilizes conservation equations for unsteady, turbulent and incompressible flow with constant properties. Using the Reynolds' decomposition [31], $u_x = \bar{u}_x + u'_x$, $u_r = \bar{u}_r + u'_r$ and $T = \bar{T} + T'$. The corresponding equations for time-averaged continuity, axial and radial momentum, and energy, respectively, are expressed for the fluid region as [32]

$$\frac{\partial \bar{u}_x}{\partial x} + \frac{1}{r} \frac{\partial (r \bar{u}_r)}{\partial r} = 0, \tag{1}$$

$$\begin{aligned} \rho \left(\frac{\partial \bar{u}_x}{\partial t} + \bar{u}_x \frac{\partial \bar{u}_x}{\partial x} + \bar{u}_r \frac{\partial \bar{u}_x}{\partial r} \right) = & -\frac{\partial P}{\partial x} + 2 \frac{\partial}{\partial x} \left(\mu \frac{\partial \bar{u}_x}{\partial x} \right) + \frac{1}{r} \\ & \times \frac{\partial}{\partial r} \left(r \mu \left(\frac{\partial \bar{u}_x}{\partial r} + \frac{\partial \bar{u}_r}{\partial x} \right) \right) \\ & - \rho \left\langle \frac{\partial u_x'^2}{\partial x} + \frac{\partial (u_x' u_r')}{\partial r} + \frac{u_x' u_r'}{r} \right\rangle + \rho g, \end{aligned} \tag{2}$$

$$\begin{aligned} \rho \left(\frac{\partial \bar{u}_r}{\partial t} + \bar{u}_x \frac{\partial \bar{u}_r}{\partial x} + \bar{u}_r \frac{\partial \bar{u}_r}{\partial r} \right) = & -\frac{\partial P}{\partial r} + \frac{\partial}{\partial x} \left(\mu \left(\frac{\partial \bar{u}_x}{\partial r} + \frac{\partial \bar{u}_r}{\partial x} \right) \right) \\ & + 2 \frac{1}{r} \frac{\partial}{\partial r} \left(r \mu \frac{\partial \bar{u}_r}{\partial r} \right) - 2 \mu \frac{\bar{u}_r}{r^2} \\ & - \rho \left\langle \frac{\partial (u_x' u_r')}{\partial x} + \frac{\partial u_r'^2}{\partial r} + \frac{u_r'^2}{r} \right\rangle, \end{aligned} \tag{3}$$

and

$$\frac{\partial \bar{T}}{\partial t} + \bar{u}_x \frac{\partial \bar{T}}{\partial x} + \bar{u}_r \frac{\partial \bar{T}}{\partial r} = \frac{\partial}{\partial x} \left(\alpha \frac{\partial \bar{T}}{\partial x} - \langle u_x' T' \rangle \right) + \frac{1}{r} \frac{\partial}{\partial r} \left(\alpha r \frac{\partial \bar{T}}{\partial r} - r \langle u_r' T' \rangle \right). \tag{4}$$

The standard two-equation $k - \epsilon$ turbulent model, as prescribed in the ANSYS Guide [23], is used to provide closure to the unresolved Reynolds stress terms. The fluctuating terms are expressed in terms of the gradients of the mean quantities in accordance with the eddy viscosity hypothesis, where the eddy viscosity, μ_t , is expressed as

$$\mu_t = \frac{C_\mu \rho k^2}{\epsilon}. \tag{5}$$

The kinetic energy and dissipation energy equations are given, respectively, by

$$\begin{aligned} 2 \nabla \cdot \mu \langle \vec{\nabla} s_{ij} \rangle = & \frac{\partial}{\partial x} \mu \left\{ \frac{\partial k}{\partial x} + \frac{\partial \langle u_x'^2 \rangle}{\partial x} + \frac{1}{r} \frac{\partial r \langle u_x' u_r' \rangle}{\partial r} \right\} \\ & + \frac{1}{r} \frac{\partial}{\partial r} \mu r \left\{ \frac{\partial k}{\partial r} + \frac{\partial \langle u_x' u_r' \rangle}{\partial x} + \frac{1}{r} \frac{\partial r \langle u_r'^2 \rangle}{\partial r} \right\} \end{aligned} \tag{6}$$

and

$$\epsilon = \frac{2}{\rho} \mu \langle \langle s_{ij} s_{ij} \rangle \rangle, \tag{7}$$

where

$$s_{ij} = \frac{\partial u_r'}{\partial x} + \frac{\partial u_x'}{\partial r}. \tag{8}$$

The boundary conditions are specified as follows. Velocity and liquid temperature in the reservoir inlet are assumed uniform and adjusted according to values of the film's Reynolds and Prandtl number: $U = \nu Re / D_H$, $V = 0$, and $T = T_{in}(Pr)$ for $x = -1060$ mm and -12.7 mm $\leq r \leq -6.6$ mm. The outlet condition at the bottom of the domain is assumed to be uniform pressure equal to atmosphere to conform to experimental conditions. Also to conform to the data, a constant heat flux is applied along the lower stainless steel portion of the test section that results in a temperature rise equal to that produced experimentally across the thermally-developing span of the film, $-k_s \partial T / \partial r = q_w''$ for $0 \leq x \leq 781$ mm.

The interfacial treatment considers the influences of surface tension and molecular viscosity, and neglects the vapor shear at the film interface. The tangential and normal force balance equations at the film surface are always satisfied. The curvature terms in these equations are calculated in each cell by FLUENT from the volume fraction gradients, as per the continuum surface force model proposed by Brackbill et al. [33]. These tangential and normal forces perturb the interface, and instabilities are amplified by the turbulent nature of the flow.

At the wall, surface tension effects are considered by prescribing wall adhesion in terms of contact angle. The viscosity-influenced near-wall region is completely resolved all the way to the viscous sublayer, and both ϵ and turbulent viscosity are specified. This region is further subdivided into a viscosity-influenced region and a fully turbulent region, whose separation is determined by a wall-distance-based turbulent Reynolds number. In the fully turbulent region, the $k - \epsilon$ model is employed to define turbulent viscosity, while the one-equation model of Wolfstein [34] is applied in the viscosity-influenced near-wall region. In the latter model, the momentum and k equations are retained, and the length scale for turbulent viscosity is derived according to Chen and Patel [35]. Jongen [36] derived a technique for smoothly blending this two-layer definition for turbulent viscosity with the high Reynolds number definition from the outer region. FLUENT utilizes this two-layer model with a modified single function formulation of the law of the wall for the entire wall region by blending laminar and turbulent law of the wall relations as per Kader [37]. This formulation guarantees correct asymptotic behavior for large and small values of y^+ and reasonable representation of velocity profiles where y^+ falls inside the buffer region. This method involves modification of the fully turbulent relation and takes into account other effects such as pressure gradients or variable properties. The walls are governed by continuities of both temperature and heat flux, and the wall heat flux is applied by conduction normal to the fluid body.

Two-phase treatment follows the Volume of Fluid (VOF) model [38]. From an examination of turbulence models presented in [7], and following numerical turbulence studies by Kays [39], a constant turbulent Prandtl number value of $Pr_t = 1$ is used. The constant C_μ in Eq. (5) is set equal to 0.09. The porous film distributor has a porosity of 0.002 and a viscous resistance of 3.846×07 m⁻². In order to conserve computation time, the

fractional step version of the non-iterative time advancement (NITA) scheme is used with first-order implicit discretization at every time-step [40,41] to obtain pressure–velocity coupling. Gradient generation during spatial discretization is accomplished using the least-squares cell-based scheme [42], while PRESTO, QUICK, Geo-reconstruct and first-order upwind schemes [43] are used for pressure, momentum, volume fraction and turbulent kinetic energy resolution, respectively.

The grid system consists of 401,426 nodes and 397,111 cells, which is arrived at after careful assessment in pursuit of optimum degree of mesh refinement. This process involves evaluating the influence of mesh size on computational effort and quality of results. The grid system used is non-uniform, with a larger number of grid points near the wall, film interface, porous zone and heated portion of the test section to achieve superior accuracy in resolving key flow parameters. Although the bulk flow region of the falling film is modeled using a mesh size estimated to capture turbulence quite well, an order of magnitude refinement in the mesh is adopted beginning well outside the narrow viscous layer at the interface to ensure high resolution in capturing turbulence at the interface. It is important to note that the transition in refinement is gradual to avoid influencing the flow.

4. Statistical results

4.1. Statistical approach

The method adopted in this study to explore the statistical parameters of the falling liquid film consists of (i) applying statistical functions directly to the measured temporal records of both film thickness and liquid temperature, (ii) applying identical statistical functions to the computed thickness and temperature, and (iii) comparing statistical results from the measured and computed time records as a means of validating the effectiveness of compu-

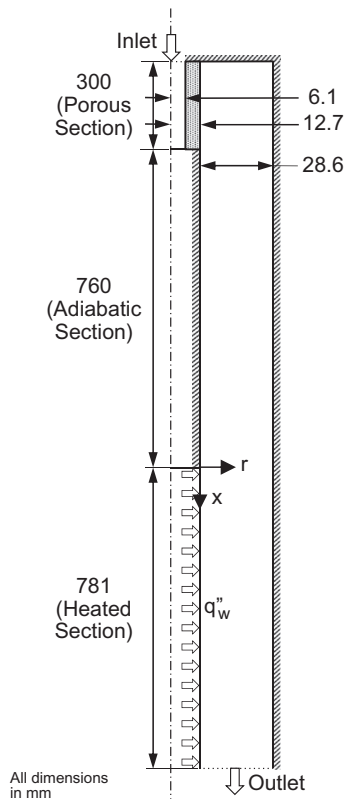


Fig. 4. Computational domain.

tational methods at capturing the interfacial profile and influence of waves on liquid temperature for free-falling turbulent liquid films.

The statistical functions are applied to temporal records similar to those shown in Fig. 1(a) and (b). These records are treated as time series and examined with the aid of statistical tools. The variables that are examined here are assumed stationary (*i.e.*, their mean and variance do not change over time) in order to apply time invariant statistical functions. It is also assumed that the variables are ergodic (*i.e.*, their average value over a long time period can be equated to the average of values obtained at different times). Presented below are probability density, covariance and spectral plots of both film thickness and interfacial temperature.

4.2. Probability density and variance results

Probability density of a variable is the representation of expectation of occurrence of all possible values of that variable. The probability distribution, $P(\delta)$, and probability density, $p(\delta)$, of film thickness, δ , are given, respectively by Anderson [44]

$$P(\delta) = \text{Prob}\{\delta(t) < \delta\} = \frac{n\{\delta(t) < \delta\}}{N} \quad (9)$$

and

$$p(\delta) = \lim_{\Delta\delta \rightarrow 0} \frac{\text{Prob}\{\delta < \delta(t) < \delta + \Delta\delta\}}{\Delta\delta} = \frac{dP(\delta)}{d\delta}, \quad (10)$$

where N and n are the total number of samples and number of samples in a subset of the time record, respectively. Fig. 5 shows the probability density of film thickness at $x = 278$ mm based on measured and numerically predicted time records for three narrow ranges of film Reynolds number between 3000 and 11,700 and four wall heat fluxes. Each of the curves based on measured records is the mean for eight data sets, each spanning 5 s, at identical operating conditions, while the curves based on computed records include every instantaneous thickness value in a 6-s interval. Unlike the mean values of film thickness and temperature presented in [7], the probability density curves provide valuable information about the manner in which these variables are distributed about the mean.

Fig. 5 clearly shows that increasing Reynolds number shifts film thickness to higher values. However, the distribution is asymmetric, with dense thickness data in the low thickness range compared to a sparser distribution in the high thickness range. Fig. 5 reveals that there is a high likelihood that the film assume a narrow range of low thickness values, and a moderate likelihood a larger range of high thickness values. The highest probability for the low, mid and high Re correspond to $\delta = 0.5$, 0.7, and 0.9 mm, respectively, and the peak probability decreases by 37.5% for every increase in Re . From these distributions, one can identify the substrate thickness and wave amplitude, and therefore surmise the interfacial character of the film. The peak probability corresponds to the most frequent thickness, which is close to the substrate thickness. The shift in the peak to the right with increasing Re indicates an increase in substrate thickness. The increase in width of distribution with increasing Re is indicative of increasing wave amplitude. Karapantsios et al. [15] obtained probability density curves for adiabatic films that are similar to those in Fig. 5, and suggested that probability density of film thickness follows the Weibull distribution for $509 \leq Re \leq 9000$ and log-normal distribution for $9000 \leq Re \leq 13,090$.

Fig. 5 shows the effects of heat flux on probability density are insignificant, with discernable decreases in peak probability density with increasing heat flux observed only for the low Re . These changes can be attributed to property variations, especially those of surface tension and viscosity. Fig. 5 also shows the probability

density based on computed thickness agrees well with that based on measured thickness. At the high Re , the distribution based on computed results is smoother, indicating more repeatable large amplitude waves. There are also slight differences in peak probability density between measured and computed results.

Another statistical parameter that is used to examine both measured and computed results is variance. Variance of a data set measures the spread of data about mean value, which, for film thickness, is defined as

$$\sigma_{\delta}^2 = \frac{1}{N} \sum_{j=1}^N [\delta_j - \bar{\delta}]^2, \tag{11}$$

where $\bar{\delta}$ is the mean, which is given by

$$\bar{\delta} = \frac{1}{N} \sum_{j=1}^N \delta_j. \tag{12}$$

Fig. 6 shows the effect of heat flux on film thickness variance, non-dimensionalized with respect to the variance for zero heat flux, based on measured and computed results. The variances of measured results for the mid and high Re peak at $q_w'' = 25,000 \text{ W/m}^2$ but increase monotonically for the low Re , a trend that is attributed

to the effects of thermocapillary forces on fluid motion [6]. The computed values increase appreciably for low heat fluxes before reaching a fairly constant value, and variance deviations for different Re values are much smaller than for the experimental values. Absent from the computed values are the distinct variance peaks achieved with the measured values for mid and high Re . The insensitivity of computed results to heat flux might be attributed to the limited extent to which they factor the influence of heat flux on fluid properties, specifically surface tension and viscosity.

Fig. 7 shows probability density for measured and computed thickness for the mid Re and seven longitudinal locations. The measured results display measurable, albeit small sensitivity to location for $x < 200 \text{ mm}$, with peak probability increasing and corresponding thickness decreasing with increasing x . The measured results are relatively insensitive to distance for $x > 200 \text{ mm}$. These trends point to substrate thinning for $x < 200 \text{ mm}$ and fully developed waviness for $x > 200 \text{ mm}$. Overall, the computed results in Fig. 7 agree well with the measured, excepting less pronounced axial variations for $x < 200 \text{ mm}$ for the computed results.

Fig. 8 shows fairly similar film thickness variance trends with x for the measured and computed results, but with the computed variance slightly smaller than the measured. Both show appreciable increases in variance upstream, reflecting the influence of

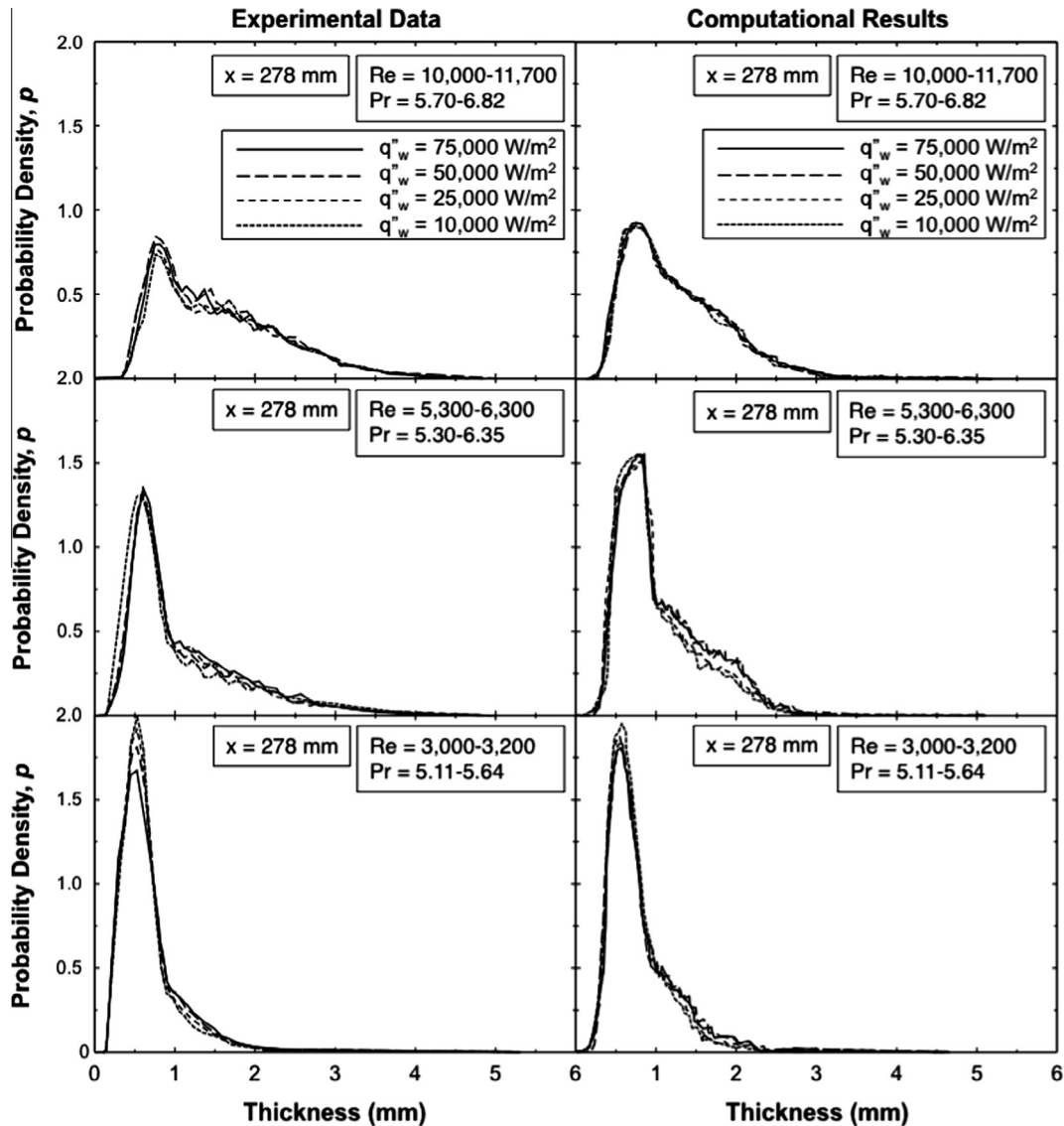


Fig. 5. Probability density of film thickness at $x = 278 \text{ mm}$ for different Reynolds numbers and heat fluxes.

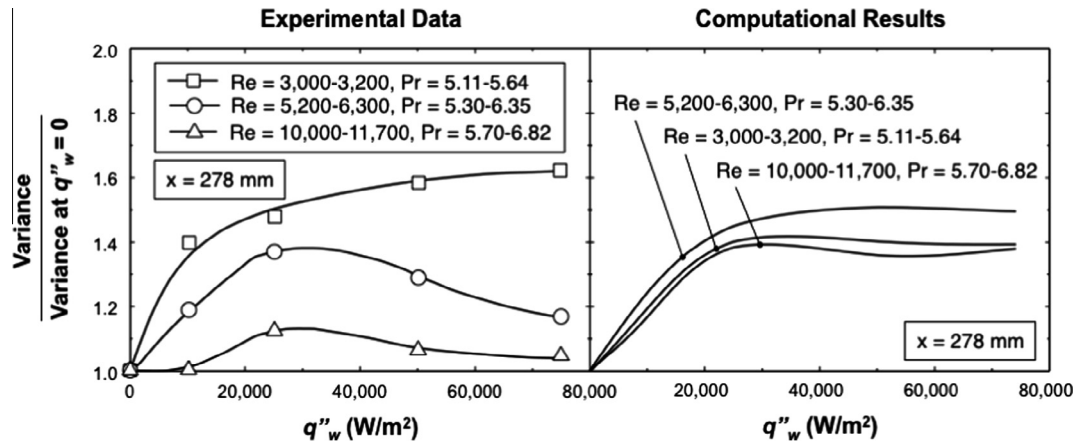


Fig. 6. Film thickness variance with heat flux at $x = 278$ mm for different Reynolds numbers.

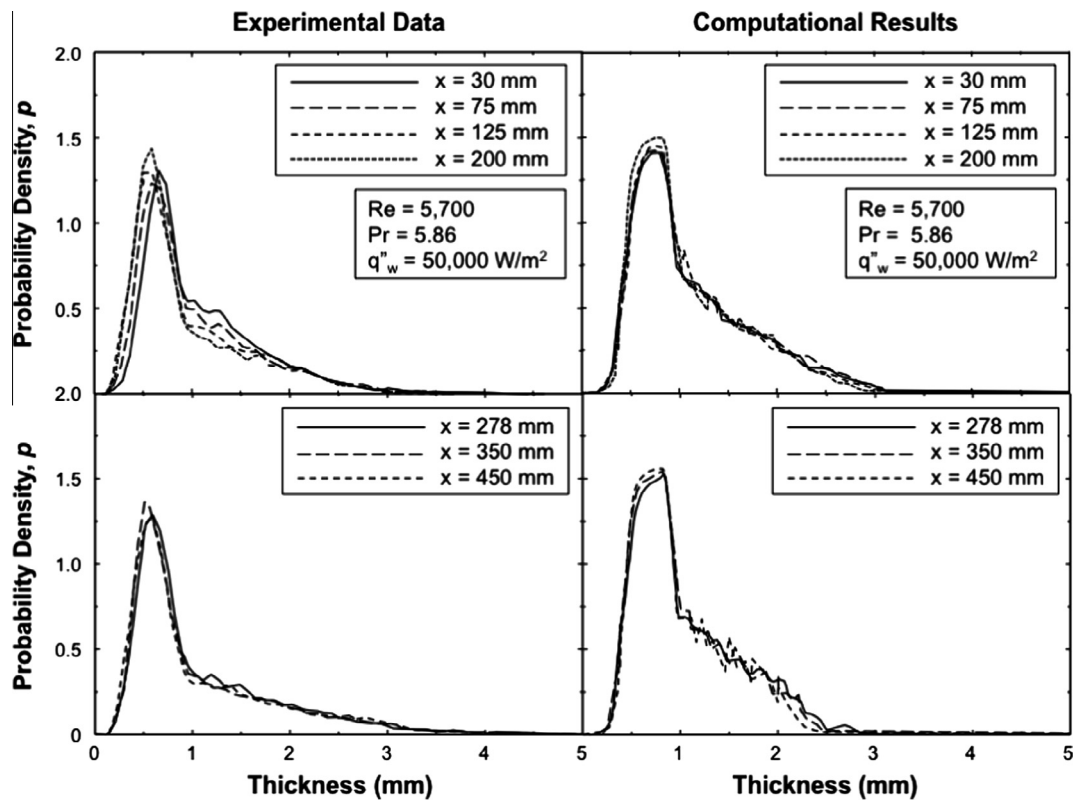


Fig. 7. Probability density of film thickness for different axial locations and $Re = 5700$, $Pr = 5.86$ and $q''_w = 50,000$ W/m².

thermal boundary layer development, and muted increases downstream, indicating rather fully developed film waviness.

Fig. 9(a) shows probability density for measured and computed difference between instantaneous and minimum interfacial liquid temperature at $x = 278$ mm for low, mid and high Re and four heat fluxes. For the measured values, the span of temperature difference is 12, 4, and 1.4 °C for the low, mid and high Re , respectively. This decrease is attributed to both larger liquid thermal mass and intensified mixing at high Re . The distribution is fairly symmetrical, implying an even split of thin film portions with high interfacial temperature fluctuations and large wave portions with small fluctuations. As expected, increasing the heat flux greatly broadens the span of interfacial temperature fluctuations.

The computational values in Fig. 9(a) match well with the measured. Notable differences are more asymmetry at high Re , coupled with a slightly reduced peak probability and wider temperature span. The asymmetry is less obvious for the mid and low Re .

Fig. 9(b) shows probability density for measured and computed difference between instantaneous and minimum interfacial liquid temperature for $Re = 5700$, $q''_w = 50,000$ W/m² and seven axial locations. The distributions show appreciable sensitivity to axial location for $x < 200$ mm but merge together for $x > 200$ mm, indicating the waviness attains fully developed character downstream. The computed results in Fig. 9(b) capture the correct trends relative to x , but with some deviation in both peak probability and temperature span.

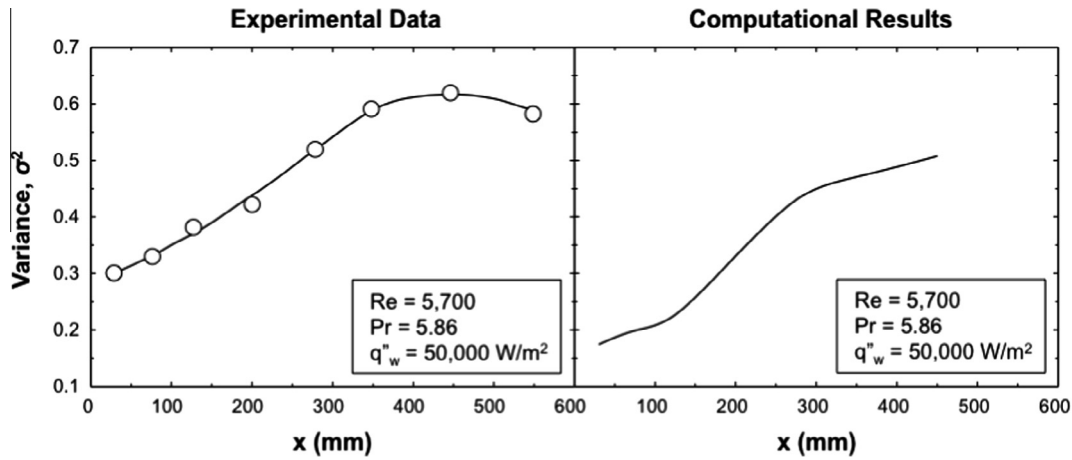


Fig. 8. Variance of film thickness with axial distance for $Re = 5700$, $Pr = 5.86$ and $q''_w = 50,000 \text{ W/m}^2$.

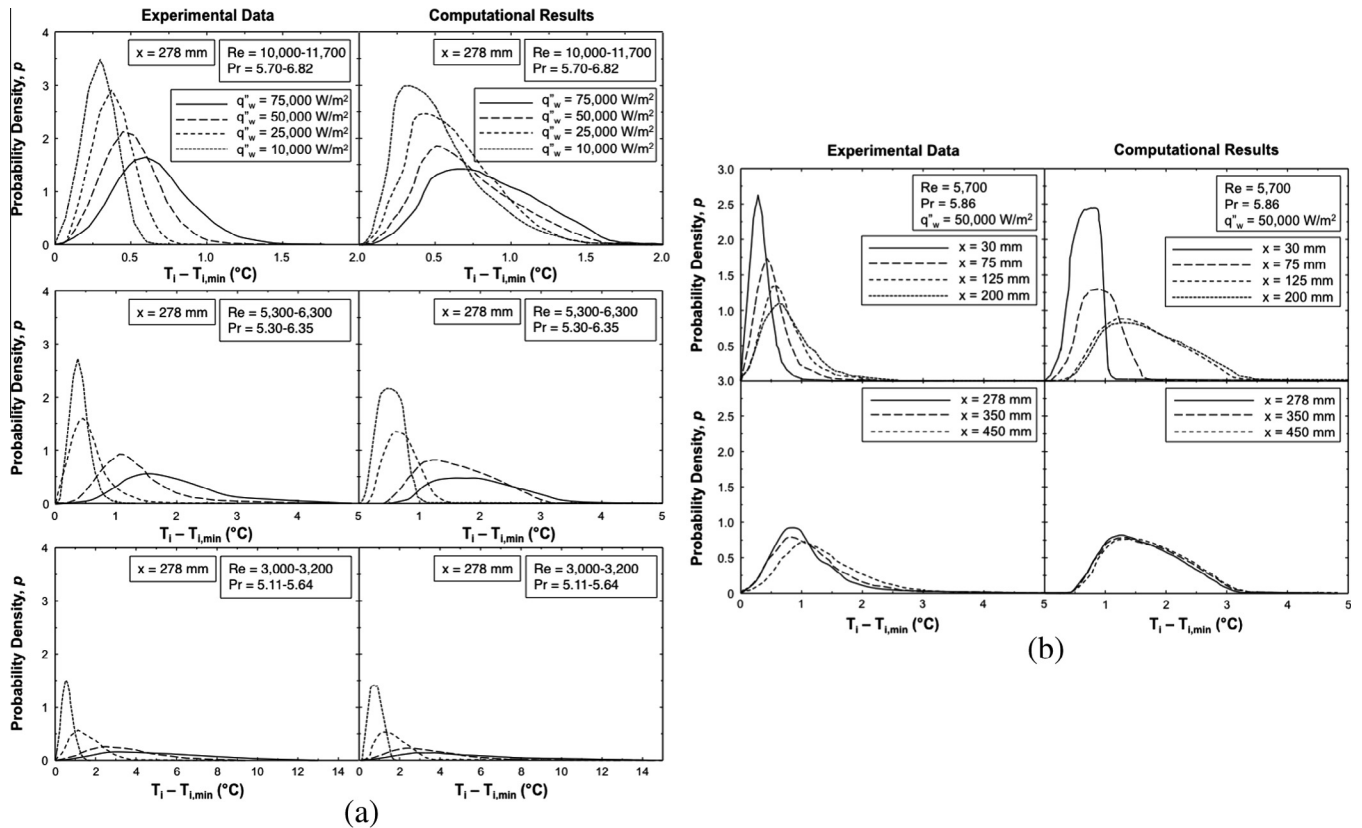


Fig. 9. Probability density of difference between instantaneous and minimum interfacial liquid temperature for (a) $x = 278 \text{ mm}$ and different Reynolds numbers and heat fluxes, and (b) $Re = 5700$, $Pr = 5.86$, $q''_w = 50,000 \text{ W/m}^2$ and different axial locations.

4.3. Auto-covariance and cross covariance results

Covariance is a measure of the tendency of two variables to co-vary or “move” together. Following [44], covariance of film thickness, δ , and difference between instantaneous and minimum interfacial temperature, $T_i - T_{i,min}$, is given by

$$cov\{\delta, T_i - T_{i,min}\} = \frac{1}{N\sqrt{\sigma_\delta^2}\sqrt{\sigma_{T_i-T_{i,min}}^2}} \sum_j (\delta_j - \bar{\delta})(T_i - T_{i,min})_j - (\bar{T}_i - \bar{T}_{i,min}), \quad (13)$$

where

$$\sigma_{T_i-T_{i,min}}^2 = \frac{1}{N} \sum_j [(T_i - T_{i,min})_j - (\bar{T}_i - \bar{T}_{i,min})]^2 \quad (14)$$

and

$$\bar{T}_i - \bar{T}_{i,min} = \frac{1}{N} \sum_{j=1}^N (T_i - T_{i,min})_j. \quad (15)$$

A positive covariance implies larger values of δ are associated with larger values of $T_i - T_{i,min}$, and smaller values of δ with smaller

values of $T_i - T_{i,min}$. A negative covariance implies smaller values of δ are associated with larger values of $T_i - T_{i,min}$, and larger values of δ with smaller values of $T_i - T_{i,min}$.

When a process has instantaneous values that are interdependent, the interdependency can be characterized with the aid of auto-covariance. For a time series, auto-covariance is the covariance between values at time t with values at other times. The auto-covariances of film thickness, δ , and difference between instantaneous and minimum interfacial temperature, $T_i - T_{i,min}$, for times t and $t + \tau$ are given, respectively, by Anderson [44]

$$R_{\delta,\delta}(\tau) = \text{cov}\{\delta(t)\delta(t + \tau)\} \quad (16)$$

and

$$R_{T_i - T_{i,min}, T_i - T_{i,min}}(\tau) = \text{cov}[T_i - T_{i,min}(t), T_i - T_{i,min}(t + \tau)], \quad (17)$$

where τ is the time “lag”. High auto-covariance indicates that the series changes slowly, or, equivalently, that the present value is predictable from previous values. For example, white noise has a very flat auto-covariance because it is random, while nature images typically possess broad spatial auto-covariance because nearby pixels are often of similar color and brightness.

Cross-covariance compares two time series by shifting one in time relative to the other. Cross-covariance between film thickness and difference between instantaneous and minimum interfacial temperature is defined as

$$C_{\delta, T_i - T_{i,min}}(\tau) = \text{cov}\{\delta(t), T_i - T_{i,min}(t + \tau)\}. \quad (18)$$

If δ and $T_i - T_{i,min}$ are delayed copies of one another, they will have a cross-correlation with a peak value of unity at some time lag. Thus, the cross-covariance is useful at capturing how interfacial temperature is influenced by interfacial waviness after some time delay.

Both the measured and computational covariance results presented here are means of discrete distributions corresponding to four data sets of identical operating conditions. The total duration for each set is 0.4 s.

Fig. 10(a) and (b) show, for the mid and high Re , respectively, both experimental and computational auto-covariance results for film thickness, δ , and difference between instantaneous and minimum interfacial temperature, $T_i - T_{i,min}$, and cross-covariance between the two parameters. The experimental auto-covariance for δ follows the pattern of a time series with periodic elements [44], starting with a value of unity for $\tau = 0$, where the thickness duplicates itself. A second relatively high positive auto-covariance value is achieved for a time lag that corresponds to the dominant wave period. Subsequent time lags that are integral multiples of the period are manifest as local maxima that gradually decline in magnitude. Consequently, local minima occur at time lags corresponding to integral multiples of the maximum out of phase value. The auto-covariance plots point to time records of film thickness that are periodic, and the phase shift at larger time lags can be attributed to the gradual influence of non-periodic elements. Notice that the periodicity is strong for both mid and high Re , and the influence of heat flux is relatively weak. However, non-periodicities for high Re are introduced much earlier, evidenced by the reduced amplitude for the larger time lags, which can be explained by the increased turbulence at high Re intensifying stochastic behavior. Fig. 10(a) and (b) show the computational results agree well with the measured, however, the maxima and minima are slightly more pronounced for the computed results.

The cross-covariance plots in Fig. 10(a) and (b) show a single significant time lag of positive covariance, followed by a somewhat neutral covariance. But most notable is a pronounced negative cross-covariance between film thickness and interfacial liquid temperature at about one quarter the wave period from the thickness auto-covariance plot. This implies that the liquid temperature

peaks in the relatively thin film region between the film substrate and wave peak, and has a minimum in the relatively thick film region between the wave peak and substrate; both behaviors are captured very well in the streamline plot in Fig. 11. Overall, cross-covariance exhibits relatively weak dependence on heat flux and the computational results show good agreement with the measured.

Fig. 12(a) and (b) show experimental and computational auto-covariance results for film thickness and difference between instantaneous and minimum interfacial liquid temperature, respectively, for $Re = 5,700$, $Pr = 5.86$ and $q_w'' = 50,000 \text{ W/m}^2$ at seven longitudinal locations. For the most part, the auto-covariance results appear to be weakly influenced by x . However, the auto-covariance of film thickness shows stronger correlation for $x > 200 \text{ mm}$, which proves that the film attains fully developed wave structure downstream. This trend is not captured in the temperature auto-covariance plots. The computed results show stronger auto-covariance for both thickness and interfacial temperature and, like the measured results, exhibit weak sensitivity to x .

4.4. Auto-spectrum and cross-spectrum results

A spectral plot is a graphical data analysis technique that is used to examine frequency domain models for single or multiple time series, and provides an alternate means to assessing covariance and periodicity. The key approach in spectral analysis is to superimpose sine and cosine profiles with different amplitudes to generate an artificial time series that resembles the actual time series. An examination of the terms that constitute the artificial series allows for easier interpretation of the actual time series.

The auto-spectrum function for a given frequency f is obtained by applying smoothed Fast Fourier Transforms (FFTs) to auto-covariance data [45], which, for film thickness, is given by

$$S_{\delta,\delta}(f) = \frac{\Delta[R_{\delta,\delta}(0)] + \sum_{j=1}^{L-1} R_{\delta,\delta}(j)w(j) \cos(2\pi f j \Delta)}{\sum_{j=1}^{L-1} R_{\delta,\delta}(0) \cos(2\pi f j \Delta)}, \quad (19)$$

where Δ , $R_{\delta,\delta}$, L and $w(j)$ are, respectively, the difference between adjacent covariance values, auto-covariance at time lag j , total number of discrete time lags used, and window function that aids in the smoothing.

The cross-spectrum for film thickness and difference between instantaneous and minimum interfacial liquid temperature is similarly obtained by applying smoothed FFTs to the cross-covariance data [45],

$$S_{T_i - T_{i,min}, T_i - T_{i,min}}(f) = \frac{\Delta[R_{T_i - T_{i,min}, T_i - T_{i,min}}(0)] + \sum_{j=1}^{L-1} R_{T_i - T_{i,min}, T_i - T_{i,min}}(j)w(j) \cos(2\pi f j \Delta)}{\sum_{j=1}^{L-1} R_{T_i - T_{i,min}, T_i - T_{i,min}}(0) \cos(2\pi f j \Delta)}. \quad (20)$$

For the experimental data, the thickness and temperature spectra are calculated in the present study following a method previously employed by Karapantsios et al. [15] in analyzing adiabatic film thickness data. A Hanning window function is applied to reduce side-lobe leakage (i.e., filter out noise in the time records) [46]. Spectral results are calculated for each of three segments of a database using an FFT code written by Newland [47], which are then averaged. Representative spectra are finally obtained by averaging results from four data bases obtained at identical operating conditions. The computational results are processed by considering eight covariance sets of 0.4 s intervals and converted to spectral plots using DATAPLOT [48], a statistical analysis tool developed by the National Institute of Standards and Technology (NIST), which is used in this study to perform the FFT, smoothing and averaging. The Tukey window function used for smoothing and to reduce leakage is given by [49]

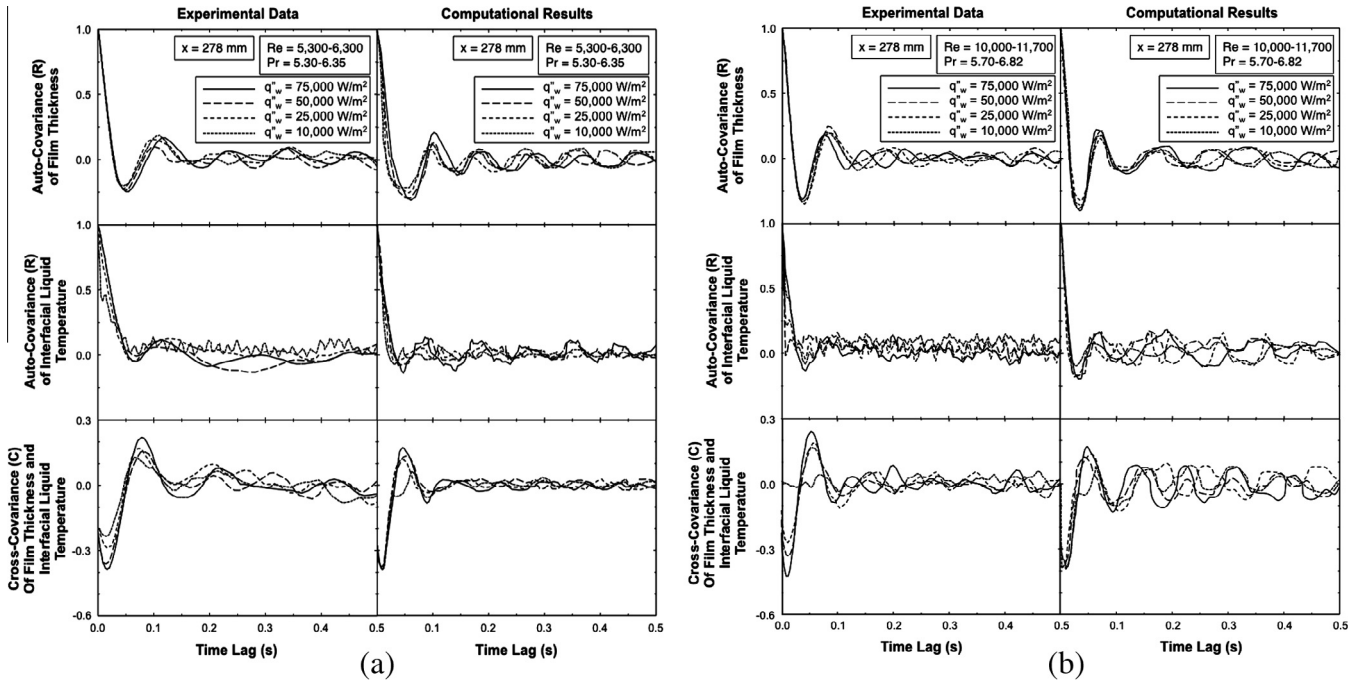


Fig. 10. Auto-covariances of film thickness and difference between instantaneous and minimum interfacial liquid temperature, and corresponding cross-covariance at $x = 278$ mm for (a) $Re = 5300\text{--}6300$ and $Pr = 5.30\text{--}6.35$, and (b) $Re = 10,000\text{--}11,700$ and $Pr = 5.70\text{--}6.82$.

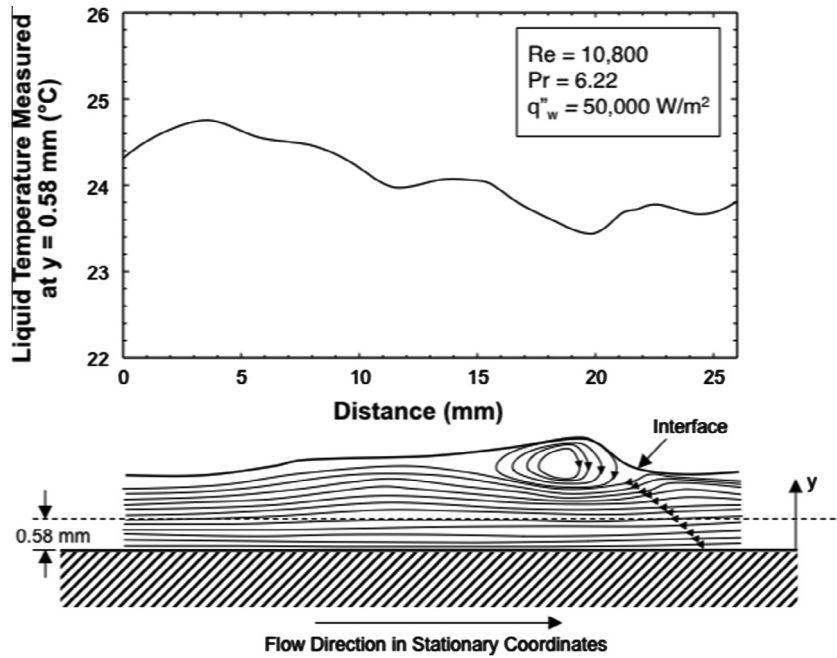


Fig. 11. Computed liquid flow streamlines and liquid temperature measured at $x = 278$ mm and $y = 0.58$ mm for $Re = 10,800$, $Pr = 6.22$ and $q_w'' = 50,000$ W/m² (adapted from [5]).

$$w(u) = \frac{1}{2} \left[1 + \cos\left(\frac{\pi u}{L}\right) \right], \quad (21)$$

and the number of time lags, L , which correlates the width N , in samples, of a discrete-time symmetrical window function $w(j)$, is calculated as [49]

$$L = \frac{N}{4} - 1. \quad (22)$$

Fig. 13(a) and (b) show experimental and computational auto-spectra of film thickness and difference between instantaneous and minimum interfacial liquid temperature, normalized by the FFT of their respective variance at zero time lag, and cross-spectra between the two parameters, normalized by the product of the FFTs of their respective variance at zero time lag, at $x = 278$ mm for different heat fluxes at mid and high Re , respectively. The thickness auto-spectra display peak values over a narrow frequency

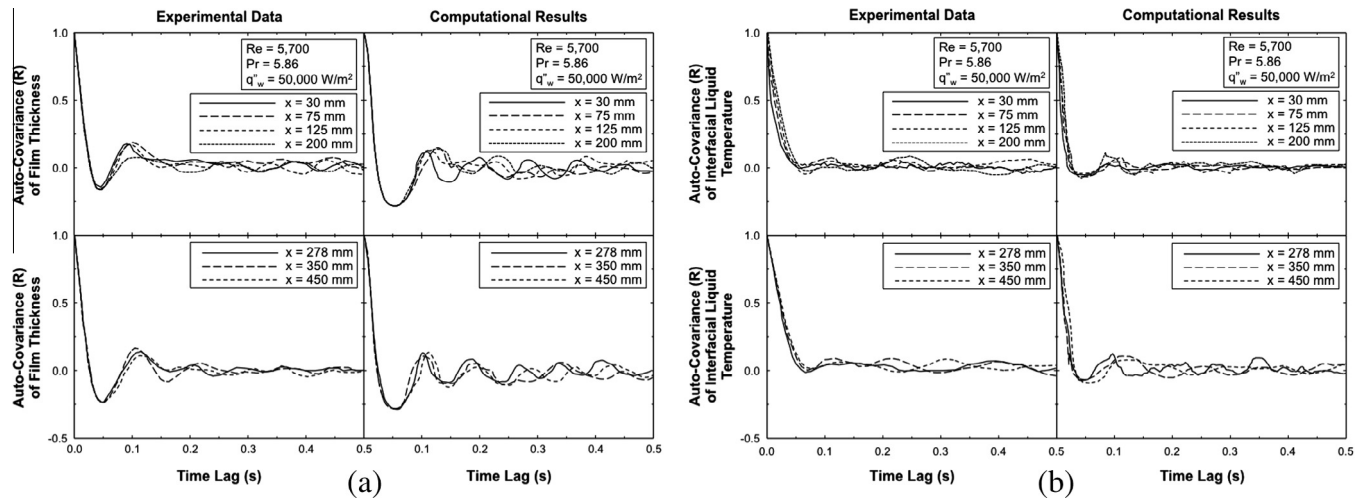


Fig. 12. Measured and computed auto-covariance results of (a) film thickness and (b) difference between instantaneous and minimum interfacial liquid temperature for $Re = 5700$, $Pr = 5.86$ and $q''_w = 50,000 \text{ W/m}^2$ at different longitudinal locations.

range. Note that every spectral point can be viewed as the variance of δ obtained for a sample time that equals $1/f$. Therefore, at moderate and high Re numbers, the peak δ variance is seen to occur for sample times of 0.125 and 0.09 s, respectively, the reciprocals of the frequencies captured in the plots. These times correspond to the periods observed in the film thickness time records, implying that the maximum variance corresponds to a time span equal to the wave period. Note that the peak auto-spectra in Fig. 13(a) and (b) span a frequency range rather than a specific frequency because the respective time records do not possess consistent periods over a long interval. As per [50], the frequency corresponding to the peak value is the modal frequency of large waves. This conclusion is consistent with the previous discussion concerning the periods identified in the thickness time records as those for the large waves. Positive slopes of the auto-spectrum are a symptom of increasing variance, and hence negative correlation of δ , and vice versa. High frequencies at which the auto-spectra progress to zero aid in identification of the characteristics of small interfacial ripples. It is also observed for the high Re that there are multiple local peaks in the vicinity of the frequency corresponding to the identifiable period of the film thickness time records. This can be explained by the early introduction of non-periodicities due to increased turbulence at high Re , which was also attributed in the previous section to the reduced amplitudes of the film thickness auto-covariance at the same Re . These non-periodicities result in the interfacial waves having a wider range of periods, and hence, multiple spectral peaks. As expected, increasing the heat flux increases the variance and hence the magnitude of the auto-spectrum. The computational results compare well with the measurements, but with a more negative slope in the low frequency region.

The auto-spectra for interfacial temperature also exhibit a local peak over a narrow frequency range, but this effect is subdued by the high values corresponding to low frequencies. These high values are indicative of high interfacial temperature variance over small time samples in the temperature time records. Fig. 13(a) and (b) show increasing flow rate and heat flux produce the same effect on the temperature auto-spectra as those for thickness. Again, computational results show good agreement with this data.

Due to the afore-mentioned phase shift between thickness and interfacial temperature, the cross-covariance magnifies covariance trends of the individual parameters. This is manifest in Fig. 13(a)

and (b), where the cross-spectra peak in the same frequency range as the auto-spectra.

Fig. 13(c) and (d) show experimental and computational auto-spectra of film thickness and difference between instantaneous and minimum interfacial liquid temperature, and cross-spectra between the two parameters for mid Re at small and large longitudinal locations, respectively. The spectral plots show high sensitivity to small x values and insignificant sensitivity to large x values. Overall, the computed results agree well with the measured.

The findings from the present study provide further evidence of the effectiveness of computational tools at predicting the complex transport phenomena associated with wavy liquid–vapor interfaces. This study also points to future research opportunities to utilize computational tools to investigate other types of wavy liquid–vapor flows, such as those associated with heated or condensing liquid films that are shear-driven by fast moving vapor flow, and flow boiling critical heat flux (CHF) that is preceded by formation of a wavy interface between a liquid core and near-wall vapor layer [51–55]. Such efforts would also benefit from experimental validation efforts including detailed measurements of liquid velocity within liquid films [56,57].

5. Conclusions

This study employed statistical tools to examine the evolution of film thickness and interfacial temperature in turbulent, free-falling water films subjected to sensible heating. Time records of thickness and temperature were measured in a film that was formed on a vertical test section fitted with an assortment of fast response measurement probes. The same time records were predicted computationally using FLUENT. The statistical tools were applied to both the measured and computed time records. Key findings from the study are as follows.

- (1) Probability density of film thickness is asymmetric, with dense data in the small thickness range and sparser data in the large. Peak probability for $Re = 3000$ – 3200 , 5300 – 6300 and 10000 – 11700 occurs at $\delta = 0.5$, 0.7 and 0.9 mm, respectively, which correspond closely to substrate thickness. There is also an increase in thickness span with increasing Re , indicating an increase in wave amplitude. Auto-covariance of thickness is effective at capturing the dominant

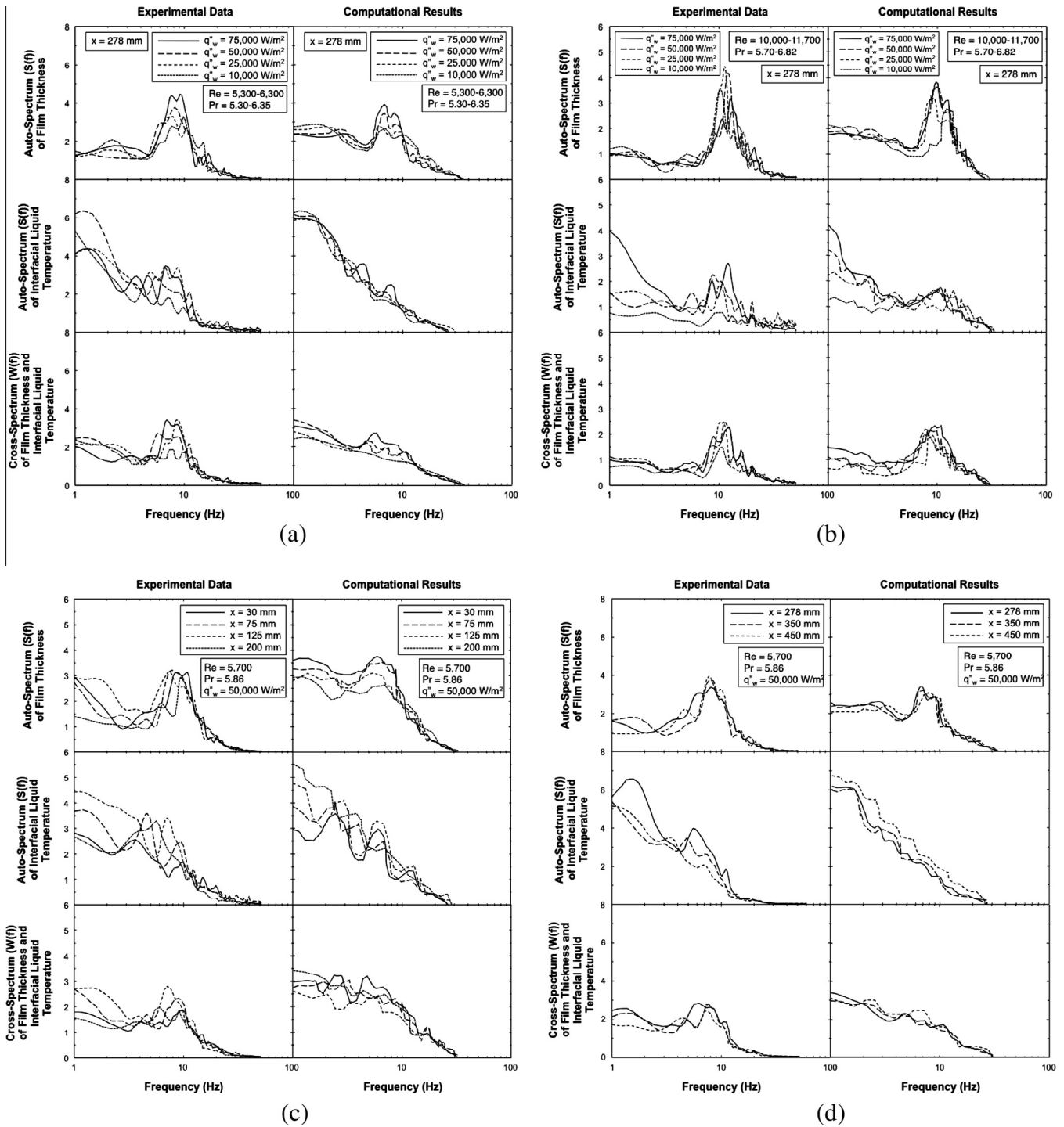


Fig. 13. Auto-spectra of film thickness and difference between instantaneous and minimum interfacial temperature, and corresponding cross-spectra for (a) $x = 278$ mm, $Re = 5300\text{--}6,300$, $Pr = 5.30\text{--}6.3$ and different heat fluxes, (b) $x = 278$ mm, $Re = 10,000\text{--}11,700$, $Pr = 5.70\text{--}6.82$ and different heat fluxes, (c) $Re = 5300\text{--}5500$, $Pr = 6.08\text{--}6.35$, $q_w'' = 50,000$ W/m² and different upstream axial locations, and (d) $Re = 5300\text{--}5500$, $Pr = 6.08\text{--}6.35$, $q_w'' = 50,000$ W/m² and different downstream axial locations.

wave period, and proves the film thickness time record is periodic. The auto-spectrum of film thickness is effective at capturing the range of dominant frequencies corresponding to the large waves.

(2) Probability density of interfacial temperature is fairly symmetrical, suggesting nearly equal number of thin substrate data with high interfacial temperature fluctuations and thick wave data with small fluctuations. Increasing Re decreases the interfacial temperature difference, a trend attributed to

both larger liquid thermal mass and intensified mixing at high Re . Increasing the wall heat flux greatly broadens the span of interfacial temperature fluctuations.

(3) Cross-covariance of film thickness and interfacial temperature difference captures a pronounced negative minimum at about one quarter the dominant wave period. This implies a clear phase shift between the two parameters, with the liquid temperature reaching a maximum in the relatively thin film region between the substrate and wave peak.

- (4) The probability density, covariance and spectra of both the film thickness and interfacial temperature difference exhibit clear dependence on axial distance for $x < 200$ mm, compared to insignificant dependence for larger distances. These trends point to a wave structure gradually developing in the thermal entrance region, and a fully developed structure downstream.
- (5) Overall, the statistical results based on computed film thickness and interfacial temperature difference agree well with the results based on the measured. This proves the effectiveness of the adopted computational tools at predicting the complex transport phenomena associated with wavy liquid–vapor interfaces.

Acknowledgement

The authors are grateful for the partial support for this project from the National Aeronautics and Space Administration (NASA) under grant no. NNX13AB01G.

References

- [1] L.-T. Yeh, R.C. Chu, Thermal Management of Microelectronic Equipment: Heat Transfer Theory, Analysis Methods, and Design Practices, ASME, New York, 2002.
- [2] T.M. Anderson, I. Mudawar, Microelectronic cooling by enhanced pool boiling of a dielectric fluorocarbon liquid, *J. Heat Transfer – Trans. ASME* 111 (1989) 752–759.
- [3] S. Mukherjee, I. Mudawar, Smart pumpless loop for micro-channel electronic cooling using flat and enhanced surfaces, *IEEE Trans. Compon. Packag. Technol.* 26 (2003) 99–109.
- [4] S. Mukherjee, I. Mudawar, Pumpless loop for narrow channel and micro-channel boiling from vertical surfaces, *J. Electron. Packag. Trans. ASME* 125 (2003) 431–441.
- [5] N. Mascarenhas, I. Mudawar, Study of the influence of interfacial waves on heat transfer in turbulent falling films, *Int. J. Heat Mass Transfer* 67 (2013) 1106–1121.
- [6] T.H. Lyu, I. Mudawar, Statistical investigation of the relationship between interfacial waviness and sensible heat transfer to a falling liquid film, *Int. J. Heat Mass Transfer* 34 (1991) 1451–1464.
- [7] N. Mascarenhas, I. Mudawar, Investigation of eddy diffusivity and heat transfer coefficient for free-falling turbulent liquid films subjected to sensible heating, *Int. J. Heat Mass Transfer* 64 (2013) 647–660.
- [8] O.M. Phillips, The equilibrium range in the spectrum of wind-generated waves, *J. Fluid Mech.* 4 (1958) 426–434.
- [9] A.S. Telles, A.E. Dukler, Statistical characteristics of thin, vertical, wavy, liquid films, *Ind. Eng. Chem. Fundam.* 9 (1970) 99–109.
- [10] K.J. Chu, A.E. Dukler, Statistical characteristics of thin wavy films: part II study of the substrate and its wave structure, *AIChE J.* 20 (1974) 695–706.
- [11] K.J. Chu, A.E. Dukler, Statistical characteristics of thin wavy films: part III structure of the large waves and their resistance to gas flow, *AIChE J.* 21 (1975) 583–593.
- [12] O.C. Jones, J.M. Delhaye, Transient and statistical measurement techniques for two-phase flows: a critical review, *Int. J. Multiphase Flow* 3 (1976) 89–116.
- [13] H. Takahama, S. Kato, Longitudinal flow characteristics of vertically falling liquid films without concurrent gas flow, *Int. J. Multiphase Flow* 6 (1980) 203–215.
- [14] F. Nencini, P. Andreussi, Studies of the behavior of disturbance waves in annular two-phase flow, *Can. J. Chem. Eng.* 60 (1982) 459–465.
- [15] T.D. Karapantsios, S.V. Paras, A.J. Karabelas, Statistical characteristics of free falling films at high Reynolds numbers, *Int. J. Multiphase Flow* 15 (1989) 1–21.
- [16] W. Ambrosini, N. Forgiato, F. Oriolo, Statistical characteristics of a water film falling down a flat plate at different inclinations and temperatures, *Int. J. Multiphase Flow* 28 (2002) 1521–1540.
- [17] J.A. Shmerler, I. Mudawar, Local heat transfer coefficient in wavy free-falling turbulent liquid films undergoing uniform sensible heating, *Int. J. Heat Mass Transfer* 31 (1988) 67–77.
- [18] T.H. Lyu, I. Mudawar, Determination of wave-induced fluctuations of wall temperature and convection heat transfer coefficient in the heating of a turbulent falling liquid film, *Int. J. Heat Mass Transfer* 34 (1991) 2521–2534.
- [19] T.H. Lyu, I. Mudawar, Simultaneous measurement of thickness and temperature profile in a wavy liquid film falling freely on a heating wall, *Exp. Heat Transfer* 4 (1991) 217–233.
- [20] J.A. Shmerler, I. Mudawar, Local evaporative heat transfer coefficient in turbulent free-falling liquid films, *Int. J. Heat Mass Transfer* 31 (1988) 731–742.
- [21] W.J. Marsh, I. Mudawar, Predicting the onset of nucleate boiling in wavy free-falling turbulent liquid films, *Int. J. Heat Mass Transfer* 32 (1989) 361–378.
- [22] R. Walraven, Digital filters, in: Proceedings Digital Equipment Computer Users Society, San Diego, CA, 1980, pp. 827–834.
- [23] ANSYS FLUENT 12.1 in Workbench User's Guide, ANSYS Inc., Canonsburg, PA, 2009.
- [24] F. Gu, C.J. Liu, X.G. Yuan, G.C. Yu, CFD simulation of liquid film flow on inclined plates, *Chem. Eng. Technol.* 27 (2004) 1099–1104.
- [25] F. Jafar, G. Thorpe, O.F. Turan, Liquid film falling on horizontal circular cylinders, in: Proceedings 16th Australasian Fluid Mech. Conf., Brisbane, Australia, 2007, pp. 1193–1199.
- [26] J.F. Xu, B.C. Khoo, N.E. Wijeysondera, Mass transfer across the falling film: simulations and experiments, *Chem. Eng. Sci.* 63 (2008) 2559–2575.
- [27] S. Bo, X. Ma, Z. Lan, J. Chen, H. Chen, Numerical simulation on the falling film absorption process in a counter-flow absorber, *Chem. Eng. J.* 156 (2010) 607–612.
- [28] C.-D. Ho, H. Chang, H.-J. Chen, C.-L. Chang, H.-H. Li, Y.-Y. Chang, CFD simulation of the two-phase flow for a falling film microreactor, *Int. J. Heat Mass Transfer* 54 (2011) 3740–3748.
- [29] F. Sun, S. Xu, Y. Gao, Numerical simulation of liquid falling film on horizontal circular tubes, *Front. Chem. Sci. Eng.* 6 (2012) 322–328.
- [30] H. Ganapathy, A. Shooshtari, K. Choo, S. Dessiatoun, M. Alshehhi, M. Ohadi, Volume of fluid-based numerical modeling of condensation heat transfer and fluid flow characteristics in microchannels, *Int. J. Heat Mass Transfer* 65 (2013) 62–72.
- [31] O. Reynolds, Study of fluid motion by means of coloured bands, *Nature* 50 (1894) 161–164.
- [32] J.O. Hinze, Turbulence, McGraw-Hill, New York, NY, 1975.
- [33] J.U. Brackbill, D.B. Kothe, C. Zemach, A continuum method for modeling surface tension, *J. Comput. Phys.* 100 (1992) 335–354.
- [34] M. Wolfstein, The velocity and temperature distribution of one-dimensional flow with turbulence augmentation and pressure gradient, *Int. J. Heat Mass Transfer* 12 (1969) 301–318.
- [35] H.C. Chen, V.C. Patel, Near-wall turbulence models for complex flows including separation, *AIAA J.* 26 (1988) 641–648.
- [36] T. Jongen, Simulation and modeling of turbulent incompressible flows (Ph.D. Thesis), EPF Lausanne, Lausanne, Switzerland, 1992.
- [37] B. Kader, Temperature and concentration profiles in fully turbulent boundary layers, *Int. J. Heat Mass Transfer* 24 (1981) 1541–1544.
- [38] C.W. Hirt, B.D. Nicholls, Volume of fluid (VOF) method for dynamics of free boundaries, *J. Comput. Phys.* 39 (1981) 201–225.
- [39] W.M. Kays, Turbulent Prandtl number where are we?, *J. Heat Transfer Trans. ASME* 116 (1994) 284–295.
- [40] S. Armsfield, R. Street, The fractional-step method for the Navier–Stokes equations on staggered grids: accuracy of three variations, *J. Comput. Phys.* 153 (1999) 660–665.
- [41] H.M. Glaz, J.B. Bell, P. Colella, An analysis of the fractional-step method, *J. Comput. Phys.* 108 (1993) 51–58.
- [42] W. Anderson, D.L. Bonhus, An implicit algorithm for computing turbulent flows on unstructured grids, *Comput. Fluids* 23 (1994) 1–21.
- [43] S.V. Patankar, Numerical Heat Transfer and Fluid Flow, Hemisphere, Washington, DC, 1980.
- [44] T.W. Anderson, The Statistical Analysis of Time Series, Wiley, New York, NY, 1958.
- [45] G.M. Jenkins, D. Watts, Spectral Analysis and its Applications, Holden-Day, San Francisco, CA, 1968.
- [46] D.E. Newland, An Introduction to Random Vibrations and Spectral Analysis, second ed., Longman, New York, NY, 1984.
- [47] J.E. Koskie, I. Mudawar, W.G. Tiederman, Parallel-wire probes for measurement of thick liquid films, *Int. J. Multiphase Flow* 15 (1989) 521–530.
- [48] J. Filliben, Dataplot—an interactive high level, language for graphics non-linear fitting, data analysis, and mathematics, in: Proceeding Third Annual Conf. National Computer Graphics Assoc., Anaheim, CA, 1982.
- [49] J. Tukey, Exploratory Data Analysis, Addison-Wesley, New York, NY, 1979.
- [50] H.T. Davis, Statistical Mechanics of Phases, Interfaces, and Thin Films, Wiley, New York, NY, 1996.
- [51] C.O. Cersey, I. Mudawar, Effects of heater length and orientation on the trigger mechanism for near-saturated flow boiling critical heat flux – I. Photographic study and statistical characterization of the near-wall interfacial features, *Int. J. Heat Mass Transfer* 38 (1995) 629–641.
- [52] C.O. Cersey, I. Mudawar, Effects of heater length and orientation on the trigger mechanism for near-saturated flow boiling critical heat flux – II. Critical heat flux model, *Int. J. Heat Mass Transfer* 38 (1995) 643–654.
- [53] J.C. Sturgis, I. Mudawar, Critical heat flux in a long, rectangular channel subjected to onesided heating – I. Flow visualization, *Int. J. Heat Mass Transfer* 42 (1999) 1835–1847.
- [54] J.C. Sturgis, I. Mudawar, Critical heat flux in a long, rectangular channel subjected to onesided heating – II. Analysis of critical heat flux data, *Int. J. Heat Mass Transfer* 42 (1999) 1849–1862.
- [55] H. Zhang, I. Mudawar, M.M. Hasan, Flow boiling CHF in microgravity, *Int. J. Heat Mass Transfer* 48 (2005) 3107–3118.
- [56] I. Mudawar, R.A. Houpt, Mass and momentum transport in smooth falling liquid films laminarized at relatively high Reynolds numbers, *Int. J. Heat Mass Transfer* 36 (1993) 3437–3448.
- [57] I. Mudawar, R.A. Houpt, Measurement of mass and momentum transport in wavy-laminar falling liquid films, *Int. J. Heat Mass Transfer* 36 (1993) 4151–4162.